Turkish Journal of Chemistry

http://journals.tubitak.gov.tr/chem/

Research Article

Turk J Chem
(2022) 46: 1897-1908

doi:10.55730/1300-0527.3489

Morphological, microstructural and photocatalytic characterization of undoped and Ni, Co doped Fe_2O_3 particles synthesized by sonochemical method

Elif EMİL-KAYA[1,2,3,*], Burak EVREN[2,3], Zeynep ERDÖL[2,4], Duygu EKİNCİ[2], Mehmet İPEKOĞLU[5], Sibel ÖZENLER[5]

[1]Department of Materials Science and Engineering, Faculty of Georesources and Materials Engineering, RWTH Aachen University, Aachen, Germany
[2]Department of Materials Science and Technology, Faculty of Science, Turkish-German University, İstanbul, Turkey
[3]Department of Metallurgical and Materials Engineering, Faculty of Chemical and Metallurgical Engineering, İstanbul Technical University, İstanbul, Turkey
[4]Department of Materials Science and Engineering, Faculty of Engineering, Gebze Technical University, Kocaeli, Turkey
[5]Department of Mechanical Engineering, Faculty of Engineering, Turkish-German University, İstanbul, Turkey

Received: 10.12.2021 • **Accepted/Published Online:** 02.08.2022 • **Final Version:** 19.12.2022

Abstract: In this study, an abundant and eco-friendly photocatalytic material, Fe_2O_3 particles were synthesized by sonochemical method. Morphological and microstructural investigations of synthesized undoped and Ni, Co-doped Fe_2O_3 particles were performed. The effect of particle morphology and microstructure on its photocatalytic performance was further investigated. Comparative studies for evaluating particle crystallite sizes were conducted by Williamson-Hall (W-H) method and modified Debye-Scherrer (MDS). Crystallite sizes and lattice strains of Fe_2O_3 induced by process parameters were calculated by W-H method based on uniform deformation model (UDM). The crystallite sizes of the synthesized powders were calculated in the range of 200 nm and 76 nm by Williamson-Hall analysis. In addition to structural investigation, dislocation density of the synthesized particles was calculated by Williamson-Smallman relation. Afterwards, photocatalytic performance of Fe_2O_3 particles was investigated in detail. The photodegradation of methylene blue solutions in the presence of light in 20 min with samples 3,4, and 5 in 20 min were 0.937, 0.896, and 0.855, respectively. Moreover, the photodegradation of methylene blue solution with sample 5 for 15, 30, and 45 min were 0.9, 0.828, and 0.757, respectively. A photocatalytic activity of 24.25% has been observed under optimum conditions for the time interval of 45 min.

Key words: Fe_2O_3, crystallite size, lattice strain, dislocation density, photocatalytic performance, Williamson-Hall analysis

1. Introduction

In recent years, pollution in wastewater, especially caused by dyes, has caused serious environmental problems. There are many organic pollutants and dyes dropped directly into water sources from the chemical, pharmaceutical and textile industries. Dyes are extensively used in various industries during material processing. It is reported that 10%–15% of consumed dyes are mixed with water sources. Dyes are mostly hazardous; therefore, it is very important for the environment to treat any sort of waste that contains these substances [1–3].

Recently, several water treatment methods have been developed. Degradation of organic substances by photocatalytic materials is a promising method for removing organic pollutants from wastewater. Semiconductor materials such as TiO_2, Al_2O_3, Sb_2O_3, Sm_2O_3, Fe_2O_3, WO_3, CeO_2, V_2O_5 have been used as photocatalytic materials in degradation of organic dies [4–16]. Among these semiconductor materials, hematite (Fe_2O_3) is abundant in earth, inexpensive and environmentally friendly. Therefore, it is mostly used in gas sensors, solar cells, lithium-ion batteries, fuel cells. Hematite also functions as photocatalytic material since it is a semiconductor [17–21]. Fe_2O_3 particles have been synthesized in various morphologies through hydrothermal [22], coprecipitation [23], solvothermal [24], spray pyrolysis [25] and sol-gel methods [26]. Photodegradation of various organics under UV light or daylight by synthesized Fe_2O_3 particles has been researched in several studies. The effect of doping elements ~~to~~ on Fe_2O_3 bandgap and photocatalytic activity has also been investigated [27].

Sivakumar et al. synthesized Ni doped Fe_2O_3 nanoparticles by chemical precipitation method. Bandgap of semiconductor is calculated from UV-Vis analysis results and reduction in bandgap with Ni doping was observed. Changes in the

* Correspondence: eemil@ime-aachen.de

magnetic hysteresis curves with doping of nickel at different rates were investigated [28]. Transition element (Cu, Ni, Co) doped Fe_2O_3 nanoparticles for photocatalytic applications were synthesized by Satheesh et al. Magnetic and photocatalytic properties of synthesized powders were investigated. It was reported that acid red 27 (AR27) degradation rate of Cu doped Fe_2O_3 particles was the highest. As solution pH is among important factors that affect photodegradation, photodegradation activity of particles synthesized at pH levels between 3 and 9 was investigated. Highest photodegradation degree of 98.05% was reported at pH 6. Effect of catalyst and organic die concentrations was also investigated [29]. Sn doped Fe_2O_3 particles were synthesized by Mansour et al. through coprecipitation method. Sn was doped at molar concentrations of 0.01%, 0.03%, and 0.06%. Reduction in crystallite size and bandgap was reported. Highest Rhodamine B (RhB) degradation rate was reported for 0.06% Sn doped Fe_2O_3 particles [30].

In many studies in the literature, the effect of Fe_2O_3 morphology on photocatalytic activity was investigated. In the study of Yan et al., Rhodamine (RhB) degradation of Fe_2O_3 particles synthesized in the form of rings was investigated under UV light in the 400–800 wavelength range [31]. In another study, photocatalytic activity of nanoplate shaped hematite particles synthesized through microwave assisted solvothermal method was investigated against salicylic acid by Sun et al. [32]. By using different precipitating agents (NaCl, NaBr), Wang et al. synthesized Fe_2O_3 particles and investigated the difference in photocatalytic activity. Particles synthesized by NaCl showed higher surface area, therefore had a higher light absorbance and photocatalytic activity was increased [33]. Photocatalytic activity of hematite produced by sol-gel method at different calcination temperatures was investigated by Boumaza et al. Calcination temperature affected the surface area and therefore altered the photochemical activity [34].

In recent years, ultrasonic waves have been preferred in many studies to synthesize different materials. When liquids are exposed to strong sound waves, high- and low-pressure waves are formed, which causes small air bubbles to form, and when the bubbles reach a certain size, they split immediately. Current and turbulence emerged this way provides on one hand a strong agitation, on the other hand a homogeneous mixture is obtained. Moreover, turbulence splits the agglomerated particles and therefore is very effective in shrinking soft and hard particles [35]. It was reported that usage of ultrasonic waves in the synthesis process instead of conventional mixing and heating methods shortened the synthesis duration.

In this study, undoped, Ni and Co-doped Fe_2O_3 particles were synthesized through various process parameters via sonochemical method. The effect of process parameters including calcination time, the amount of ethylene glycol, the addition of PVP, and Ni, Co doping on photocatalytic activity of Fe_2O_3 was revealed. The particle morphologies of the synthesized hematite particles were manipulated by process parameters. The synthesized particles phase analysis was conducted by XRD. On the basis of XRD peaks, crystallite sizes were calculated by mathematical models including W-H and MDS methods. Moreover, dislocation densities were calculated by Williamson-Smallman model. In order to investigate the short-term photocatalytic activity of the synthesized particles, photocatalytic tests were conducted by methylene blue (MB) solution under a halogen light for different durations. The photodegradation of organic dyes was characterized by a UV-Vis spectrophotometer.

2. Materials and methods

Firstly, ethylene glycol was prepared. Afterwards, 1% wt polyvinylpyrrolidone (PVP, mn: 10000) was dissolved in ethylene glycol in an ultrasonic bath. The base solution was prepared using a 200 mL ethylene glycol – PVP mixture and 100 mL deionized water. Iron nitrate, nickel nitrate and cobalt nitrate ($Fe(NO_3)_3.6H_2O$, $Ni(NO_3)_3.6H_2O$ and $Co(NO_3)_3.6H_2O$ Carlo Erba) solutions were prepared. Then, iron nitrate (0.1mol/L) solution was prepared by mixing of nickel nitrate (vol. 1.5%) and cobalt nitrate (vol. 1.5%) for producing of Ni, Co doped Fe_2O_3. Afterwards, gelation was initiated by adding ammonia (NH_4OH, Merck) to iron nitrate solution. After the beginning of gelation, solution was mixed with an ultrasonic homogenizer for 6 min. After 48 h, precipitates were filtrated and dried in the oven for 24 h. Different samples were calcined at 700 °C and 900 °C for 3 h. After calcination, Fe_2O_3 formation was observed. Experimental parameters are given in Table 1. Crystal structures of synthesized particles were analyzed by X-ray Diffractometer (Bruker AXS/Discovery D8) with monochromatic CuKα tube in the range of 10–90° within 0.02° steps and phase analyzes were conducted by X'Pert HighScore program. The effect of process parameters on crystallite sizes was conducted by Williamson-Hall analysis based on uniform deformation model. In order to compare the results obtained by Williamson-Hall analysis, the modified Debye-Scherrer method was also used to calculate crystallite sizes. Dislocation density was calculated by Williamson-Smallman analysis from the calculated crystallite sizes. In order to observe the effect of process parameters on powder morphologies, synthesized particles were analyzed by field emission gun scanning electron microscopy (FEG-SEM, Philips XL30). Methylene blue solutions (10 mg/L) were prepared to investigate the photocatalytic performances of synthesized particles. These solutions were mixed for 30 min in a dark box to reach absorption-desorption balance. Afterwards,

Table 1. Experimental parameters.

Sample	Co:Ni dop	PVP (gr)	Ethylene glycol (mL)	Cal. temp (°C)	Homogenization time (min)
Sample 1	-	-	16	900	6
Sample 2	+	-	16	900	6
Sample 3	-	1.5	100	900	6
Sample 4	-	1.5	100	700	6
Sample 5	-	3	100	700	6

hematite particles were added to methylene blue solutions with a ratio of 5 g/L. Fifty milliliters of suspension was mixed under a 100-W halogen lamp with a wavelength range of 350–1050 nm at a 15-cm distance. Samples were repeatedly taken from suspension during mixing to analyze the effect of exposure time. The catalyst material was separated from the suspension by centrifuge (Hettich, Rotina 420R). Spectral analysis was conducted by UV-Vis spectrometer (Analytikjena, Specord 200 Plus).

3. Results and discussion

3.1. Microstructural investigation of undoped and Ni, Co doped Fe_2O_3 particles

Phase analyzes of undoped and Ni, Co-doped Fe_2O_3 particles synthesized under different conditions were conducted and XRD patterns are given in Figure 1. Reference patterns of synthesized particles were determined as 01-084-0307 by X'Pert HighScore Plus software. The crystal structure of synthesized particles belongs to the rhombohedral crystal system and the space group is R-3c. Despite the changes in the production parameters, it was observed that the crystal system did not change. The determined calcination temperatures were suitable for Fe_2O_3 crystallization. Effect of process parameters on crystal sizes was conducted by Williamson-Hall analysis based on uniform deformation model. Initially, 7 peaks with high diffraction intensities were selected and peak widths were determined by X'Pert High Score Plus software. Strain-induced peak broadenings are considered as crystal defects and shown as $\varepsilon = \beta s/\tan\theta$. The equations below are derived from Scherrer and $\varepsilon = \beta s/\tan\theta$ equations. Peak broadening was calculated by subtracting instrumental peak broadening from measured peak broadening as shown in Equation 1.

$$\beta_{hkl} = [\beta^2_{measured} - \beta^2_{instrumental}]^{\frac{1}{2}} \quad (1)$$

Peak broadening consists of crystallite size and crystallite strain as shown in Equation 2.

$$\beta_{hkl} = \beta_{crystallite} + \beta_{strain} \quad (2)$$

Crystal distortion is formulated with Equation 3.

$$\varepsilon \approx \beta_s/\tan\theta \quad (3)$$

Equations 5 and 6 are derived by using Debye-Scherrer equation and equations above.

$$\beta_{hkl} = \left(\frac{k\lambda}{Dcos\theta}\right) + (4\varepsilon \tan\theta) \quad (4)$$

$$\beta_{hkl}cos\theta = \left(\frac{k\lambda}{D}\right) + (4\varepsilon \sin\theta) \quad (5)$$

β_{hkl} denotes peak broadening, θ denotes diffraction angle, whereas k denotes shape factor (in this case: 0.84), λ is the wavelength of *CuKα* radiation (λ= 0,154184 nm), *D* denotes average crystallite size and ε is average lattice strain.

β_{hkl}cosθ - 4εsinθ graph is plotted for calculating crystallite size and strain. Values were subjected to linear fitting. The slope of the line equals strain. The point where the line intercepts the y-axis equals crystallite size.

Graphs plotted by Williamson-Hall analysis are given in Figure 2.

Williamson-Hall analysis based on uniform deformation model revealed that crystallite sizes were 204, 178, 150, 107, and 76 nm, indicating that nanostructured Fe_2O_3 particles were obtained. After Ni and Co doping, a reduction in crystallite size was observed. Moreover, PVP usage reduced agglomeration during calcination and crystallite sizes were decreased with increased PVP amount. The decrement in crystallite size was observed when calcination temperature was lowered from 900 °C to 700 °C. Similar observations were reported in previous studies [36,37]. Modified Debye-Scherrer analysis was conducted to compare the results of Williamson-Hall analysis. Graphs of modified Debye-Scherrer analysis are given in Figure 3.

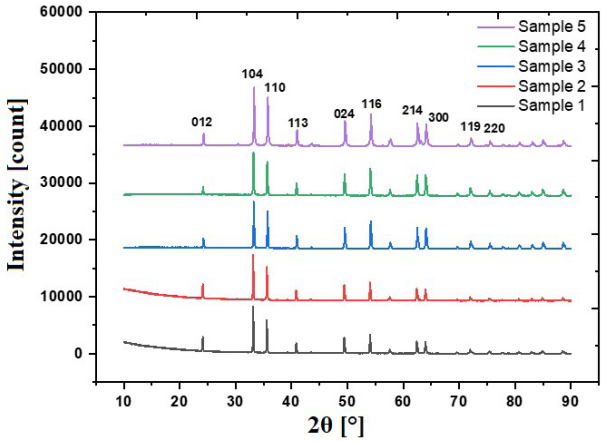

Figure 1. XRD patterns of samples 1–5.

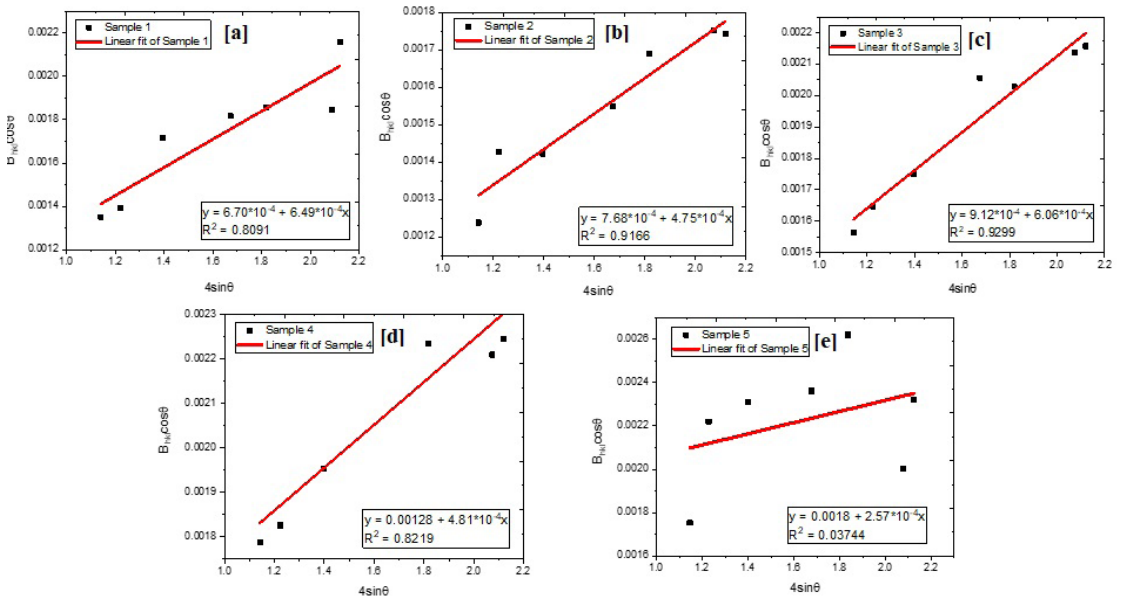

Figure 2. Williamson-Hall analyses of (a) sample 1, (b) sample 2, (c) sample 3, (d) sample 4, and (e) sample 5.

According to the modified Debye-Scherrer analysis, crystallite sizes of samples were calculated as 113, 107, 92, 79, and 67 nm. Retrieved results were relatively smaller and in accordance with Williamson-Hall's analysis. As expected, crystallite size values evaluated by the MDS method differ from the ones calculated by the W-H method owing to the negligence of the lattice strain. Due to the presence of tensile stress in the lattice, MDS method calculates smaller crystallite sizes than the W-H method. In case of compressive stresses, MDS method calculates higher crystallite sizes than the W-H method. Similar observations were reported in previous studies [38–42].

Dislocation densities were calculated by Williamson-Smallman analysis from crystallite sizes obtained by Williamson-Hall analysis. Williamson-Smallman equation is given in Equation 6.

$$\delta = \left(\frac{1}{D^2}\right) \tag{6}$$

Calculated dislocation densities and crystallite sizes are given in Table 2.

An increment in dislocation density with reduced crystallite size was observed.

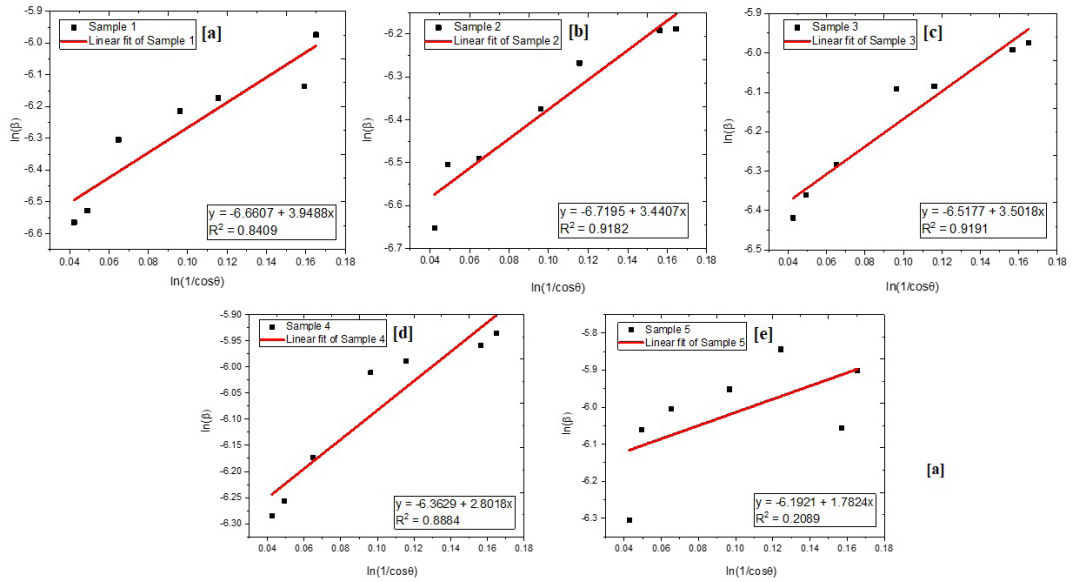

Figure 3. Modified Debye-Scherrer analyses of (a) sample 1, (b) sample 2, (c) sample 3, (d) sample 4, and (e) sample 5.

Table 2. Results of W-H and W-S analyzes.

Sample	W-H analysis (nm)	W-S analysis (δ)
Sample 1	204	2.40×10^{-5}
Sample 2	178	3.15×10^{-5}
Sample 3	150	4.44×10^{-5}
Sample 4	107	8.73×10^{-5}
Sample 5	76	1.73×10^{-4}

3.2. Investigation of powder morphologies of undoped, Ni and Co-doped Fe_2O_3 particles

In order to investigate the effects of process parameters on powder morphology, scanning electron microscopy imaging was conducted. Figure 4 represents SEM images with secondary electrons images of undoped, Ni and Co-doped Fe_2O_3 particle.

From scanning electron microscopy images, it was observed that synthesized Fe_2O_3 particles were agglomerated during the calcination step. In Ni and Co-doped samples, linear voids on grains were caused by doping elements. PVP agent was added and calcination temperature was decreased for reducing agglomeration. In order to compare the effect of PVP addition and calcination temperature, samples 3, 4, and 5 were imaged by scanning electron microscopy at different magnifications. Figure 5 illustrates SEM images with secondary electrons images of samples 3, 4, and 5.

Ethylene glycol and PVP were used to prevent to agglomeration of particles. In particular, PVP was used to encapsulate particles. Samples synthesized by the sonochemical route and contained PVP were not agglomerated and had a porous structure. Agglomeration behavior was not observed when the calcination temperature was lowered. Moreover, at lower calcination temperatures, samples obtained a spherical morphology.

3.3. Investigation of photocatalytic performance of undoped, Ni and Co doped Fe_2O_3 particles

In order to investigate the effect of powder morphology and microstructure on photocatalytic performance, photocatalysis experiments were conducted comparatively at different durations.

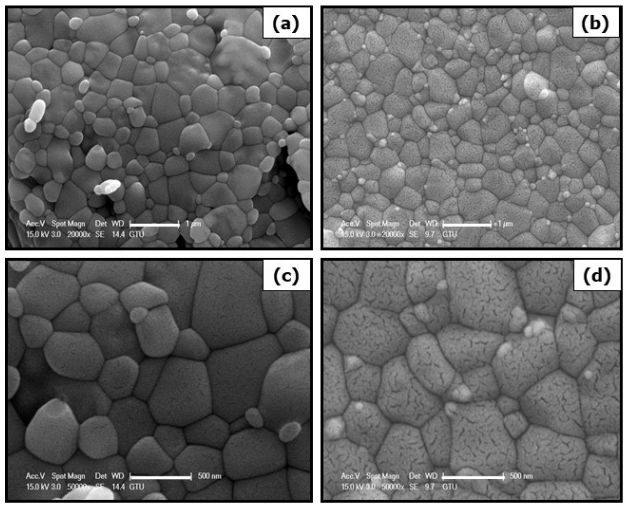

Figure 4. SEM images with secondary electrons of synthesized samples (a), (c) undoped Fe_2O_3 (sample 1) and (b), (d) Ni, Co doped Fe_2O_3 (sample 2).

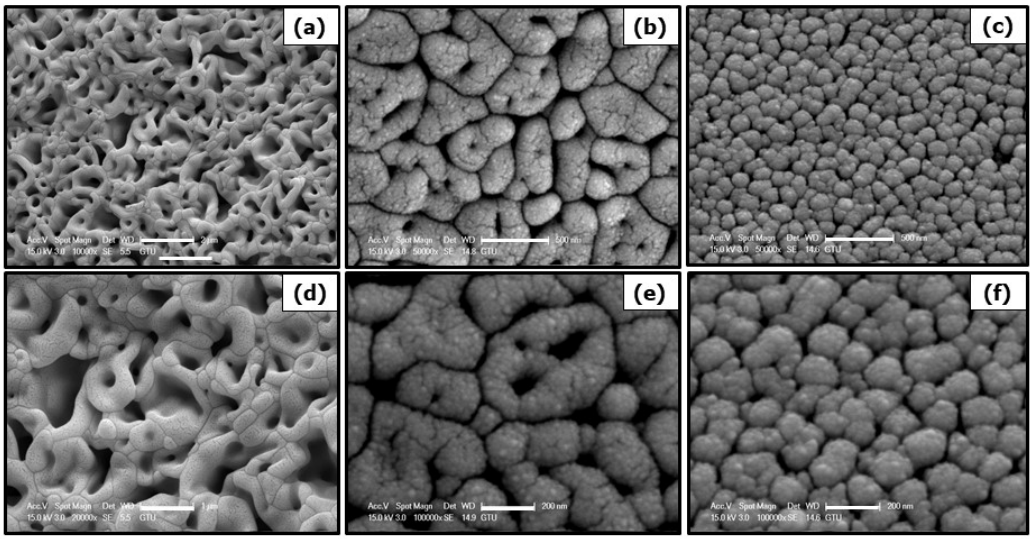

Figure 5. SEM images with secondary electrons of synthesized samples (a), (d) sample 3 (b), (e) sample 4 and (c), (f) sample 5.

Initially, photocatalysis experiments of agglomerated particles were conducted and their results are given in Figure 6.

According to UV-Vis spectrums of samples 1 and 2, particles did not exhibit photocatalytic performance. These particles were proven to be agglomerated from SEM imaging and agglomeration was considered to affect photocatalytic performance dramatically. In order to investigate the photocatalyst performances of not agglomerated particles, comparative UV-Vis spectrums of samples 3, 4, and 5 were plotted and results are given in Figure 7.

Samples 3, 4, and 5 were subjected to photocatalysis experiments for 20 min. The best performance was obtained from sample 5, which was not agglomerated during the calcination step. Investigating the SEM images and XRD patterns, sample 5 had a lower particle size than other samples. According to Williamson-Hall analysis, sample 5 had the lowest crystallite size. As sample 5 showed the highest photocatalytic activity, in order to investigate the effect of light exposure duration, it was exposed to halogen light for 45 min and changes in the absorbance with time is measured by UV-Vis spectrometer. UV-Vis spectrum is given in Figure 8.

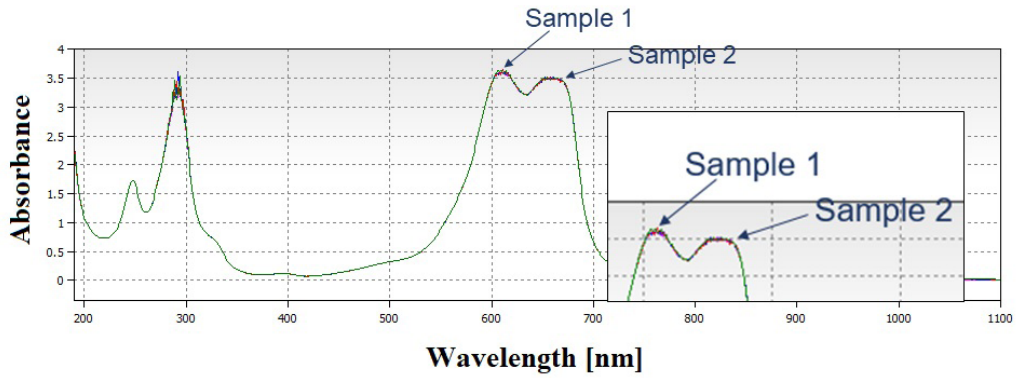

Figure 6. UV-Vis spectrum of MB and photocatalysis experiment results of samples 1 and 2.

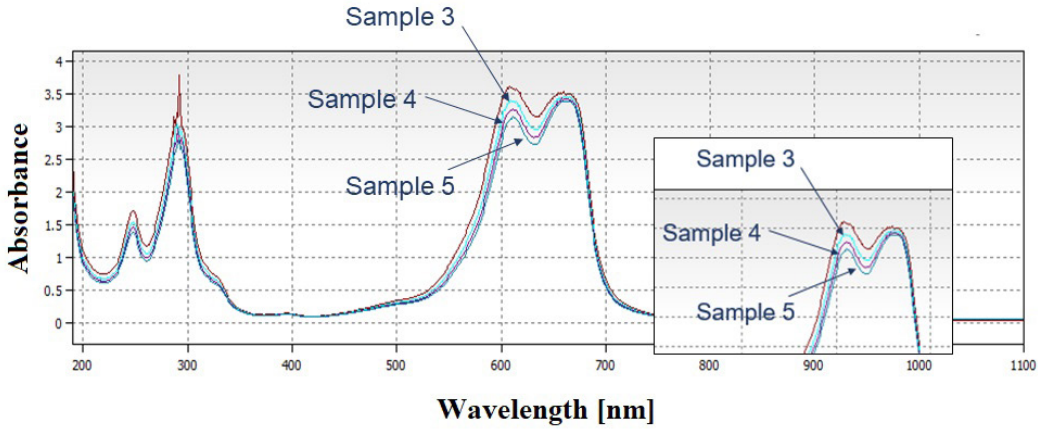

Figure 7. UV-Vis spectrum of MB and photocatalysis experiment results of samples 3, 4, and 5.

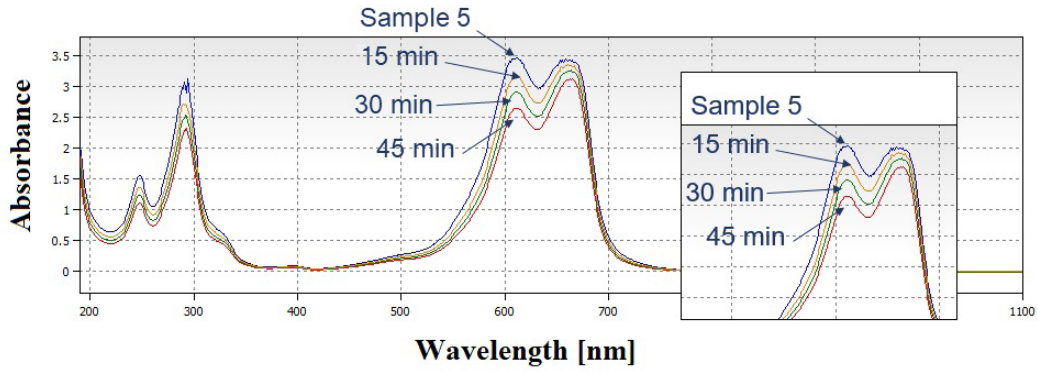

Figure 8. UV-Vis spectrum of MB and photocatalysis experiment results of sample 5 exposed to light for 15, 30, and 45 min.

An increment in methylene blue degradation was observed with a prolonged photocatalytic activity experiment. The effect of particle morphology and microstructural properties on photocatalytic performance was investigated and although the crystallite sizes were able to be decreased by doping elements, agglomerated particles did not show photocatalytic activity. Particles with porous shapes that were not agglomerated exhibited highest photocatalytic activity.

The photodegradation of MB in the presence of light by samples 3, 4, and 5 for 20 min was calculated. Figure 9a, represents the photodegradation of MB in the presence of light by samples 3, 4, and 5 for 20 min. Figure 9b illustrates the photodegradation rate for time interval of 45 min.

From the photodegradation results of sample 3,4, and 5, it is clear that sample 5 shows higher photocatalytic rate than samples 3 and 4. Therefore, sample 5 was chosen for the prolonged photodegradation experiment. Moreover, the photodegradation of methylene blue solution with sample 5 for 15, 30 and 45 min were 0.9, 0.828, and 0.757, respectively. Figure 10 shows linearly fitted curve of $\ln(C_0/C)$ as a function of irradiation time for sample 5.

A linear behavior of Figure 10 shows the pseudo first order degradation kinetics. The slope of linear fit of this graph is 0.006, this value indicates the reaction constant.

The efficiency of the photocatalytic activity is calculated from the formula:

$$\text{Rate of degradation} = \frac{A_{(i)} - A_{(t)}}{A_{(i)}} \times 100$$

Table 3 illustrates the efficiency of the degradation of MB by samples 3, 4, and 5 in 20 min.

The efficiency of photodegradation of MB by samples 3, 4, and 5 were 6.20%, 10.30%, 14.50%, respectively, in 20 min. Table 4 represents the efficiency of the degradation of MB by sample 5 for the time interval of 45 min.

Sample 5 exhibited the photocatalytic activity with 10%, 17.15%, and 24.25% for the durations of 15, 30, and 45 min, respectively. In particular, sample 5 exhibited the better MB degradation property with 24.25% efficiency in 45 min.

Keerthana et al. investigated the photocatalytic efficiencies of Fe_2O_3, 2% Co-doped Fe_2O_3, and 4% Co-doped Fe_2O_3. The 4% Co- Fe_2O_3 sample illustrated the better dye degradation with 92% efficiency in 120 min. Moreover, the photocatalytic efficiency of Fe_2O_3, 2% Co-doped Fe_2O_3, and 4% Co-doped Fe_2O_3 were approximately 10%, 16.6%, and 30% in 40 min, respectively. Increasing the amount of cobalt favored the increase of the photocatalytic activity of the samples [43]. In another study, Ilkme et al. investigated the effect of transition metals such as Co, Ni, and Cu on the photocatalytic activity of Fe_2O_3-V_2O_5 binary oxide. The addition of transition metal improved the photocatalytic activity of the binary oxide and the addition of Cu exhibited the highest percentage of 2,4-dichlorophenol degradation (100%) in 30 min. Particularly, compared to the photocatalytic activity of pure Fe_2O_3, the improved photocatalytic activity of Cu doped Fe_2O_3-V_2O_5 could be ascribed to the addition of Cu and V_2O_5 [44]. Gu et al. studied the effect of the addition of PVP on the photocatalytic activity of TiO_2, the presence of PVP in the sol-gel process has been proved to be efficient in the photodegradation of methylene red under UV light [45]. Similarly, Phuruangrat et al. evaluated the effect of weight contents of PVP in the solutions on the synthesized photocatalytic BiOCl powders. The synthesized BiOCl nanoplate powders with PVP addition exhibit photodegradation of Rhodamine B (RhB) under visible light irradiation compared to BiOCl nanoplates without PVP addition. The weight content of PVP was ascribed to play a significant role in the morphology and size of BiOCl powders. BiOCl nanoplate powders with PVP addition exhibited the best photocatalytic efficiency for RhB photodegradation of 97.61% in 240 min [46]. Similarly, in our work, the addition of PVP plays a significant role in the photodegradation of MB and Fe_2O_3 powders with PVP addition showed the best degradation efficiency of MB.

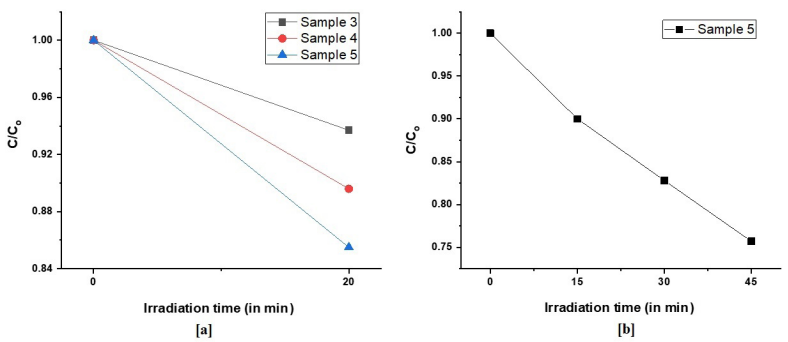

Figure 9. (a) Photodegradation of MB in the presence of light by samples 3, 4, and 5 for 20 min. (b) Photodegradation of MB in the presence of light by sample 5 for 15, 30, and 45 min.

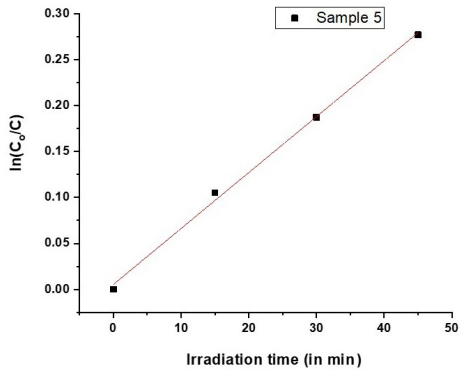

Figure 10. Linearly fitted curve of $\ln(C_0/C)$ as a function of time for sample 5.

Table 3. The efficiency of the photodegradation of samples 3, 4, and 5 in 20 min.

Sample	**Photocatalytic efficiency in 20 min (%)**
Sample 3	6.20
Sample 4	10.30
Sample 5	14.50

Table 4. The efficiency of the degradation of MB by sample 5 for the time interval 45 min.

	Photocatalytic efficiency (%)		
	15 min	**30 min**	**45 min**
Sample 5	10	17.15	24.25

4. Conclusion

In this study, undoped Fe_2O_3 and Ni and Co-doped Fe_2O_3 particles were synthesized from $Fe(NO_3)_3$ solution via sonochemical method. SEM image of the synthesized particles revealed that samples 1 and 2 were agglomerated during calcination. Samples 3, 4, and 5 had a porous structure due to PVP addition since PVP encapsulated the synthesized particles. The change in the calcination temperature from 900°C to 700°C prevented the agglomeration. The crystal structure of particles was identified as rhombohedral by XRD analysis. In order to investigate the effect of process parameters on microstructural properties, Williamson-Hall, modified Debye-Scherrer analyzes were conducted based on the XRD peak broadenings. The crystallite size of agglomerated sample 1 was calculated at 204 nm, in Co and Ni-doped samples, crystallite size is reduced as cobalt and nickel atomic radii were smaller than iron. PVP addition during synthesis prevented agglomeration and reduced the crystallite sizes. Moreover, lowering the calcination temperature prevented the formation of tensile stresses in lattice and crystallite sizes were reduced. The crystallite size of sample 5 was calculated at 76 nm. The crystallite sizes were also calculated by modified Debye-Scherrer analysis and as this calculation did not involve lattice strains, results differed from Williamson-Hall analysis, however, the results were parallel for both methods. The dislocation densities were calculated by Williamson-Smallman analysis. An increment in dislocation density was observed with reduced crystallite size. The agglomerated particles with reduced crystallite size by doping elements still did not show photocatalytic activity. Particles with a porous shape exhibited the highest photocatalytic activity. The photodegradation of MB solutions in the presence of light in 20 min with samples 3, 4, and 5 in 20 min were 0.937, 0.896, and 0.855, respectively. Moreover, the photodegradation of MB solution with sample 5 for 15, 30, and 45 min were 0.9, 0.828, and 0.757, respectively. A photocatalytic activity of 24.25% has been observed under optimum conditions for the time interval of 45 min.

Acknowledgment
This study was supported by Turkish-German University Scientific Research Projects Commission under the grant no 2018BF0021.

References

1. Guivarch E, Trevin S, Lahitte C, Oturan MA. Degradation of azo dyes in water by electro-Fenton process. Environmental Chemistry Letters 2003; 1 (1): 38-44 https://doi.org/10.1007/s10311-002-0017-0
2. Molinari R, Palmisano L, Drioli E, Schiavello M. Studies on various reactor configurations for coupling photocatalysis and membrane processes in water purification. Journal of Membrane Science 2002; 206 (1-2): 399-415 https://doi.org/10.1016/S0376-7388(01)00785-2
3. Ilisz I, Dombi A, Mogyorósi K, Farkas A, Dékány I. Removal of 2-chlorophenol from water by adsorption combined with TiO2 photocatalysis. Applied Catalysis B: Environmental 2002; 39 (3): 247-256 https://doi.org/10.1016/S0926-3373(02)00101-7
4. Mora ES, Barojas EG, Rojas ER, González RS. Morphological, optical and photocatalytic properties of TiO2–Fe2O3 multilayers. Solar energy materials and solar cells 2007; 91 (15-16): 1412-1415 https://doi.org/10.1016/j.solmat.2007.05.010
5. Liu WJ, Zeng FX, Jiang H, Zhang XS, Li WW. Composite Fe2O3 and ZrO2/Al2O3 photocatalyst: preparation, characterization, and studies on the photocatalytic activity and chemical stability. Chemical Engineering Journal 2012; 180: 9-18 https://doi.org/10.1016/j.cej.2011.10.085
6. Fu X, Tang W, Ji L, Chen S. V2O5/Al2O3 composite photocatalyst: preparation, characterization, and the role of Al2O3. Chemical Engineering Journal 2012; 180: 170-177 https://doi.org/10.1016/j.cej.2011.11.032
7. Kaplan SS, Sonmez MS. Single step solution combustion synthesis of hexagonal WO3 powders as visible light photocatalysts. Materials Chemistry and Physics 2020; 240: 122152 https://doi.org/10.1016/j.matchemphys.2019.122152
8. Liu DN, He G H, Zhu L, Zhou WY, Xu YH. Enhancement of photocatalytic activity of TiO2 nanoparticles by coupling Sb2O3. Applied surface science 2012; 258 (20): 8055-8060 https://doi.org/10.1016/j.apsusc.2012.04.171
9. Putri N, Yulizar Y, Umar A, Apriandanu DOB. Sm2O3 nanoparticles preparation using caesalpinia pulcherrima leaf extract, characterization and photocatalytic activity. In IOP Conference Series: Materials Science and Engineering Vol. 902, No. 1, p. 012012. 2020. IOP Publishing.
10. Zheng X, Li X, Peng H, Wen J. Ag-decorated core-shell Sm2O3@ TiO2 nanocomposites with enhanced visible-light photocatalytic performance. Journal of Physics and Chemistry of Solids 2018; 123: 206-215 https://doi.org/10.1016/j.jpcs.2018.07.022
11. Moongraksathum B, Yu-Wen C. CeO2–TiO2 mixed oxide thin films with enhanced photocatalytic degradation of organic pollutants. Journal of Sol-Gel Science and Technology 2017; 82(3): 772-782 DOI 10.1007/s10971-017-4355-6
12. Sinirtas E, Isleyen M, Soylu GSP. Photocatalytic degradation of 2, 4-dichlorophenol with V2O5-TiO2 catalysts: Effect of catalyst support and surfactant additives. Chinese Journal of Catalysis 2016; 37(4): 607-615 https://doi.org/10.1155/2019/1540271
13. Ozturk B, Soylu GSP. Promoting role of transition metal oxide on ZnTiO3–TiO2 nanocomposites for the photocatalytic activity under solar light irradiation. Ceramics International 2016; 42(9): 11184-11192. https://doi.org/10.1016/j.ceramint.2016.04.027
14. Saravanakumar K, Ramjan MM, Suresh P, Muthuraj V. Fabrication of highly efficient visible light driven Ag/CeO2 photocatalyst for degradation of organic pollutants. Journal of Alloys and Compounds 2016; 664: 149-160 https://doi.org/10.1016/j.jallcom.2015.12.245
15. Saravanan R, Gupta VK, Mosquera E, Gracia F. Preparation and characterization of V2O5/ZnO nanocomposite system for photocatalytic application. Journal of Molecular Liquids 2014; 198: 409-412 https://doi.org/10.1016/j.molliq.2014.07.030
16. Luu CL, Nguyen QT, Ho ST, Nguyen T. Characterization of the thin layer photocatalysts TiO2 and V2O5-and Fe2O3-doped TiO2 prepared by the sol–gel method. Advances in Natural Sciences: Nanoscience and Nanotechnology 2013; 4 (3): 035003 https://doi.org/10.1088/2043-6262/4/3/035003
17. Cavas M, Gupta RK, Al-Ghamdi AA, Gafer ZH, El-Tantawy F et al. Preparation and characterization of dye sensitized solar cell based on nanostructured Fe2O3. Materials Letters 2013; 105: 106-109 https://doi.org/10.1016/j.matlet.2013.04.053
18. Kılıç B, Gedik N, Mucur SP, Hergul AS, Gür E. Band gap engineering and modifying surface of TiO2 nanostructures by Fe2O3 for enhanced-performance of dye sensitized solar cell. Materials Science in Semiconductor Processing, 2015; 31: 363-371 https://doi.org/10.1016/j.mssp.2014.12.020
19. Reddy MV, Yu T Sow, CH Shen, ZX Lim CT, Subba Rao GV et al. α-Fe2O3 nanoflakes as an anode material for Li-ion batteries. Advanced Functional Materials 2007; 17 (15): 2792-2799 https://doi.org/10.1002/adfm.200601186
20. Lin YM, Abel PR, Heller A, Mullins CB. α-Fe2O3 nanorods as anode material for lithium ion batteries. The Journal of Physical Chemistry Letters 2011; 2 (22): 2885-2891 doi.org/10.1021/jz201363j

21. Chen J, Xu L, Li W, Gou X. α-Fe2O3 nanotubes in gas sensor and lithium-ion battery applications. Advanced Materials 2005; 17 (5): 582-586 https://doi.org/10.1002/adma.200401101

22. Colombo C, Palumbo G, Di Iorio E, Song X, Jiang Z et al. Angelico R. Influence of hydrothermal synthesis conditions on size, morphology and colloidal properties of Hematite nanoparticles. Nano-Structures & Nano-Objects 2015; 2: 19-27 https://doi.org/10.1016/j.nanoso.2015.07.004

23. Sun Y, Guo G, Yang B, Zhou X, Liu Y et al. One-step fabrication of Fe2O3/Ag core–shell composite nanoparticles at low temperature. Journal of Non-Crystalline Solids 2011; 357(3): 1085-1089 https://doi.org/10.1016/j.jnoncrysol.2010.11.031

24. Li Z, Luan P, Zhang X, Qu Y, Raziq F et al. Prolonged lifetime and enhanced separation of photogenerated charges of nanosized α-Fe2O3 by coupling SnO2 for efficient visible-light photocatalysis to convert CO2 and degrade acetaldehyde. Nano Research 2017; 10(7): 2321-2331 DOI 10.1007/s12274-017-1427-4

25. Suryavanshi RD, Mohite SV, Bagade AA, Rajpure KY. Photoelectrocatalytic activity of immobilized Fe2O3 photoelectrode for degradation of salicylic acid and methyl orange dye under visible light illumination. Ionics 2018; 24(6): 1841-1853 https://doi.org/10.1007/s11581-017-2340-2

26. Mirzaei A, Janghorban K, Hashemi B, Bonyani M, Leonardi SG et al. A novel gas sensor based on Ag/Fe2O3 core-shell nanocomposites. Ceramics International 2016; 42(16): 18974-18982 https://doi.org/10.1016/j.ceramint.2016.09.052.

27. Mishra M, Chun DM. α-Fe2O3 as a photocatalytic material: A review. Applied Catalysis A: General 2015; 498: 126-141 https://doi.org/10.1016/j.apcata.2015.03.023

28. Sivakumar S, Anusuya D, Khatiwada CP, Sivasubramanian J, Venkatesan A et al. Characterizations of diverse mole of pure and Ni-doped α-Fe2O3 synthesized nanoparticles through chemical precipitation route. Spectrochimica Acta Part A: Molecular and Biomolecular Spectroscopy 2014; 128: 69-75 doi: 10.1016/j.saa.2014.02.136

29. Satheesh R, Vignesh K, Suganthi A, Rajarajan M. Visible light responsive photocatalytic applications of transition metal (M= Cu, Ni and Co) doped α-Fe2O3 nanoparticles. Journal of environmental chemical engineering 2014; 2(4): 1956-1968 https://doi.org/10.1016/j.jece.2014.08.016

30. Mansour H, Bargougui R, Autret-Lambert C, Gadri A, Ammar S. Co-precipitation synthesis and characterization of tin-doped α-Fe2O3 nanoparticles with enhanced photocatalytic activities. Journal of Physics and Chemistry of Solids 2018; 114: 1-7 https://doi.org/10.1016/j.jpcs.2017.11.013

31. Yan X, Wu Y, Li D, Luo C, Wang Y et al. Facile synthesis of ring-like α-Fe 2 O 3 assembly composed of small hematite particles for highly efficient photocatalysis. Journal of Materials Science: Materials in Electronics 2018; 29 (4): 2610-2617 https://doi.org/10.1007/s10854-017-8186-6

32. Sun TW, Zhu YJ, Qi C, Ding GJ, Chen F et al. α-Fe2O3 nanosheet-assembled hierarchical hollow mesoporous microspheres: microwave-assisted solvothermal synthesis and application in photocatalysis. Journal of colloid and interface science 2016; 463: 107-117. https://doi.org/10.1016/j.jcis.2015.10.038

33. Wang C, Huang Z. Controlled synthesis of α-Fe2O3 nanostructures for efficient photocatalysis. Materials Letters 2016; 164: 194-197. https://doi.org/10.1016/j.matlet.2015.10.152

34. Boumaza S, Kabir H, Gharbi I, Belhadi A, Trari M. Preparation and photocatalytic H2-production on α-Fe2O3 prepared by sol-gel. international journal of hydrogen energy 2018; 43(6): 3424-3430. https://doi.org/10.1016/j.ijhydene.2017.07.227

35. Inoue M, Okada F, Sakurai A, Sakakibara M. A new development of dyestuffs degradation system using ultrasound. Ultrasonics sonochemistry 2006; 13 (4): 313-320 https://doi.org/10.1016/j.ultsonch.2005.05.003

36. Kaya EE, Ünal F, Kazmanlı K, Gürmen S. Fabrication and characterization of Yb-doped Y2O3 powders and thin films. International Journal of Materials Research 2020; 111 (7): 559-566 https://doi.org/10.3139/146.111913

37. Unal F, Kaya F. Modelling of relation between synthesis parameters and average crystallite size of Yb2O3 nanoparticles using Box-Behnken design. Ceramics International 2020; 46 (17): 26800-26808 https://doi.org/10.1016/j.ceramint.2020.07.155

38. Emil E, Gürmen S. Estimation of yttrium oxide microstructural parameters using the Williamson–Hall analysis. Materials Science and Technology 2018; 34 (13): 1549-1557 https://doi.org/10.1080/02670836.2018.1490857

39. Zak AK, Majid WA, Abrishami ME, Yousefi R. X-ray analysis of ZnO nanoparticles by Williamson–Hall and size–strain plot methods. Solid State Sciences 2011; 13 (1): 251-256. https://doi.org/10.1016/j.solidstatesciences.2010.11.024

40. Uvarov V, Popov I. Metrological characterization of X-ray diffraction methods for determination of crystallite size in nano-scale materials. Materials characterization 2007; 58 (10): 883-891 https://doi.org/10.1016/j.matchar.2006.09.002

41. Akl AA, Mahmoud SA, Al-Shomar SM, Hassanien AS. Improving microstructural properties and minimizing crystal imperfections of nanocrystalline Cu2O thin films of different solution molarities for solar cell applications. Materials Science in Semiconductor Processing 2018; 74: 183-192 https://doi.org/10.1016/j.mssp.2017.10.007

42. Kaya EE, Gürmen S. A straightforward approach for the synthesis of nanostructured Y2O3 particles: Synthesis, morphology, microstructure and crystal imperfection. Physica E: Low-dimensional Systems and Nanostructures 2020; 115: 113668 https://doi.org/10.1016/j.physe.2019.113668

43. Keerthana SP, Yuvakkumar R, Ravi G, Kumar P, Elshikh MS et al. A strategy to enhance the photocatalytic efficiency of α-Fe2O3. Chemosphere 2021; 270: 129498 https://doi.org/10.1016/j.chemosphere.2020.129498

44. Ilkme ES, Soylu GSP. The role of some metal ions in enhancement of photocatalytic activity of Fe2O3 –V2O5 binary oxide. Turkish Journal of Chemistry 2021; 45 (2): 348-361. https://doi.org/10.3906/kim-2008-57

45. Wang W, Gu M, Jin Y. Effect of PVP on the photocatalytic behavior of TiO2 under sunlight. Materials Letters 2003; 57 (21): 3276-3281. https://doi.org/10.1016/S0167-577X(03)00047-8

46. Sikder M, Wang J, Poulin BA, Tfaily MM, Baalousha M. Nanoparticle size and natural organic matter composition determine aggregation behavior of polyvinylpyrrolidone coated platinum nanoparticles. Environmental Science: Nano 2020; 7 (11): 3318-3332. https://doi.org/10.1039/D0EN00659A